Soft Matter



PAPER



Cite this: *Soft Matter,* 2016, **12**, 8774

Received 3rd August 2016, Accepted 29th September 2016

DOI: 10.1039/c6sm01790h

www.rsc.org/softmatter

Holographic characterization of colloidal fractal aggregates

Chen Wang,^a Fook Chiong Cheong,^b David B. Ruffner,^b Xiao Zhong,^c Michael D. Ward^c and David G. Grier*^a

In-line holographic microscopy images of micrometer-scale fractal aggregates can be interpreted with an effective-sphere model to obtain each aggregate's size and the population-averaged fractal dimension. We demonstrate this technique experimentally using model fractal clusters of polystyrene nanoparticles and fractal protein aggregates composed of bovine serum albumin and bovine pancreas insulin.

1 Introduction

Holograms of micrometer-scale colloidal spheres obtained with in-line holographic video microscopy can be analyzed with the Lorenz-Mie theory of light scattering to obtain each sphere's radius and refractive index, typically with part-per-thousand precision.^{1,2} Characterizing a single sphere requires a few milliseconds on a standard computer,³ which is fast enough that several thousand spheres can be characterized in under ten minutes. Analyzing holograms of aspherical particles and colloidal clusters is substantially more challenging, particularly if no information is available a priori about the particles' geometry. We previously have demonstrated that the Lorenz-Mie analysis developed for homogeneous spheres also yields useful characterization data for porous spheres,^{5,6} dimpled spheres,⁷ and protein aggregates.8 The last of these applications treats each irregularly-shaped protein aggregate as an effective sphere composed of the aggregate itself and the fluid medium filling its pores. Here, we develop an effective-sphere formalism for Lorenz-Mie microscopy of fractal aggregates and demonstrate its efficacy through measurements on model systems.

Detecting and characterizing micrometer-scale aggregates is useful both for fundamental research and also for solving real-world problems. Protein aggregation, for example, is a critical concern for the biopharmaceutical industry because it limits the efficacy of protein-based drugs and can induce harmful immunogenic responses in patients. Information on the concentration, size distribution and morphology of protein aggregates provides guidance for formulating stable products and for avoiding

2 Lorenz-Mie characterization

Lorenz–Mie characterization, depicted schematically in Fig. 1(a), is based on in-line holographic video microscopy, 12 in which the sample is illuminated with a collimated laser beam. Light scattered by a particle interferes with the remainder of the illumination in the focal plane of a microscope. The intensity $I(\mathbf{r})$ of the magnified interference pattern is recorded with a conventional video camera for analysis. A typical example is shown in Fig. 1(b). Each holographic snapshot is corrected for the camera's dark count, $I_{\rm d}$, and is normalized by the background intensity in the field of view, $I_{\rm 0}(\mathbf{r})$, to obtain 1,2,13

$$b(\mathbf{r}) = \frac{I(\mathbf{r}) - I_{\rm d}}{I_0(\mathbf{r}) - I_{\rm d}}.$$
 (1)

The normalized hologram then is fit to the prediction¹

$$b(\mathbf{r}) = |\hat{x} + e^{-ikz_p} \mathbf{f}_s(k(\mathbf{r} - \mathbf{r}_p)|a_p, n_p)|^2, \tag{2}$$

where k is the wavenumber of light in the medium, \mathbf{r}_p is the position of the particle's center relative to the center of the microscope's focal plane, and $\mathbf{f}_s(k\mathbf{r}|a_p,n_p)$ is the Lorenz–Mie function that describes scattering of the incident wave by a sphere of radius a_p and refractive index n_p . ^{14,15} The form of eqn (2)

adverse clinical outcomes. Conventional light-scattering techniques do not work well for particles in the relevant size range, ¹⁰ and cannot distinguish aggregates of interest from other contaminants commonly found in commercial formulations. Similar detection and characterization challenges arise in the precision slurries used by the semiconductor manufacturing for chemical-mechanical planarization. ¹¹ As a particle-resolved measurement technique, holographic characterization naturally differentiates micrometer-scale particles by size and composition. ³ The effective-sphere model extends these capabilities to include assessment of particle morphology without sacrificing speed or ease of use.

^a Department of Physics and Center for Soft Matter Research, New York University, New York, NY 10003, USA. E-mail: david.grier@nyu.edu; Fax: +1 (212) 995-4016; Tel: +1 (212) 998-3713

^b Spheryx, Inc., 333 E. 38th St., New York, NY 10016, USA

^c Department of Chemistry and Molecular Design Institute, New York University, New York, NY 10003. USA

Paper Soft Matter

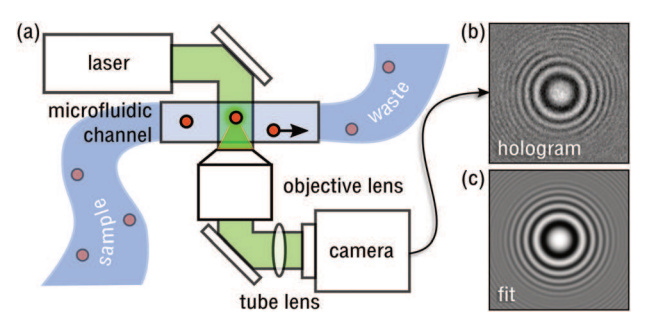


Fig. 1 (a) Lorenz–Mie characterization. A colloidal sample flowing down a microfluidic channel is illuminated by a collimated laser beam. Light scattered by a colloidal particle in the stream is collected by an objective lens and projected by a tube lens onto the sensor of a video camera, where it interferes with the unscattered portion of the beam to create a hologram. (b) The experimentally recorded hologram for a typical colloidal polystyrene aggregate. (c) Fit of the hologram in (b) to the Lorenz–Mie prediction from eqn (2).

is appropriate for a beam propagating along \hat{z} that is linearly polarized along \hat{x} . Fitting eqn (2), pixel by pixel, to the normalized hologram of a sphere yields the sphere's three-dimensional position, its radius and its refractive index. Fig. 1(c) presents the result of fitting to the experimental hologram from Fig. 1(b).

The custom-built holographic microscope used for this study illuminates the sample with the collimated beam from a solid state laser (Coherent Cube) operating at a vacuum wavelength of λ = 447 nm. The sample flows through the observation volume in microfluidic channel created by bonding the edges of a number 1.5 glass microscope cover slip to the face of a standard glass microscope slide. This sample cell is mounted on a translation stage (Prior, Proscan II) in the focal plane of an oil-immersion objective lens (Nikon, Plan Apo, 100×, numerical aperture 1.45). Light collected by the objective lens is relayed by an achromatic tube lens to a video camera (NEC, TI-324AII), which records its intensity 30 times per second with an effective magnification of 135 nm per pixel. Each video frame is a 640 pixel \times 480 pixel measurement of $I(\mathbf{r})$ with a resolution of 8 bits per pixel. Features associated with dispersed particles are identified in digitized holographic images¹⁶ and are analyzed with eqn (1) and (2) using methods that have been described in detail elsewhere.^{2,3} The example in Fig. 1(b) is a 201 pixel \times 201 pixel region of interest cropped from the normalized hologram, $b(\mathbf{r})$, obtained from $I(\mathbf{r})$ according to eqn (1).

All principal results were reproduced using a second instrument based on a 40× air objective (Nikon Plan Fluor, numerical aperture 0.75) operating at a vacuum wavelength of 532 nm (Thorlabs, CPS532 4.5 mW) with an effective magnification of 120 nm per pixel on an Allied Vision Mako U-130B camera. This camera yields 1280 pixel \times 1024 pixel images with 8 bits per pixel. Samples flow through this instrument in prefabricated microfluidic channels with 100 μm path length (Ibidi, $\mu Slide\ VI$, uncoated). Flow is driven by a syringe pump (New Era Systems, NE 100). This reduces the possibility that instrumental artifacts might have influenced the scaling relationships reported here.

A colloidal sample is characterized by placing a 100 μL aliquot in the reservoir at one end of the microfluidic channel

and drawing it through with a small pressure gradient. The resulting Poiseuille flow has a peak speed along its axis of $\nu=150~\mu m~s^{-1}$, which is small enough to avoid artifacts due to motion blurring and allows each particle to be recorded several times during its transit. Given a concentration on the order of 10^7 particles per mL, a few thousand particles will pass through the observation volume in 5 min.

A single snapshot of an individual colloidal particle can be analyzed in several milliseconds using standard computer hardware.^{3,17} Characterization data therefore can be acquired in real time as particles flow down the microfluidic channel.¹⁷ The images in Fig. 2(a) show eight stages of the transit of a typical polystyrene aggregate at 1/15 s intervals. The resulting time series of position and characterization data can be linked into a trajectory using maximum likelihood methods.^{17,19} The scatter plot in Fig. 2(b) shows the estimated values for the radius and refractive index obtained at each stage of the aggregate's trajectory, recorded at 1/30 s intervals. These results can be combined into a trajectory-averaged estimate for the associated particle's characteristics.

When this measurement technique is applied to spherical particles, the standard deviation of the trajectory-averaged characteristics is comparable to the single-measurement precision. 2,17 Results for the irregularly-shaped aggregate in Fig. 2 vary more substantially. The standard deviation of the radius, $\Delta a_{\rm p}=0.04~\mu{\rm m}$ is a factor of 10 larger than the single-measurement precision. The standard deviation of the refractive index, by contrast, is comparable to the single particle precision, $\Delta n_{\rm p}=0.002$. It is possible that the variation in apparent size occurs because the aggregate

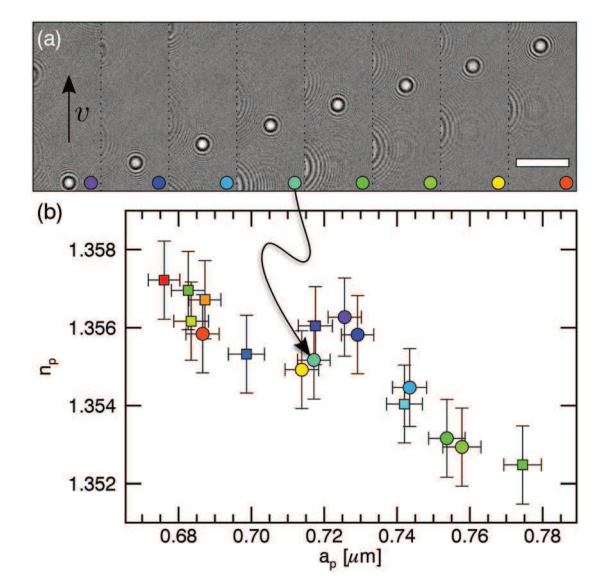


Fig. 2 Tracking and characterizing a colloidal polystyrene aggregate. (a) Eight holographic snapshots at 1/15 s intervals of an aggregate moving from the bottom of the microscope's field of view to the top at $v=120~\mu m \, s^{-1}$. The scale bar represents $20~\mu m$ in the imaging plane. (b) Fit values for the radius, $a_{\rm p}$, and refractive index, $n_{\rm p}$, obtained from the sequence of sixteen holograms recorded at 1/30 s intervals during the aggregate's 0.5 s transit. Error bars represent uncertainties in the fit values. Results from the images in (a) are plotted as circles and are interleaved with intervening results that are plotted as squares. Symbols are colored by time, as indicated by circles superimposed on the images.

Soft Matter Paper

is irregularly shaped, tumbles as it travels, and so presents different-sized projections to the instrument. We develop this interpretation in the next section.

3 Effective sphere model

Rather than attempting to generalize eqn (2) to account for the detailed structure of random colloidal aggregates, we instead analyze their holograms with eqn (2) itself and interpret the results with effective medium theory. The radius, a_p^* , and refractive index, n_p^* , obtained from such a fit then characterize an effective sphere enclosing both the fractal aggregate and also the intercalated fluid medium. The goal of the present work is to establish a relationship between the measured properties of the effective sphere and the underlying properties of the actual aggregate. This relationship then enables Lorenz–Mie microscopy to probe the morphology of fractal aggregates without incurring the computational burden of detailed modeling.

For simplicity, we assume that a fractal aggregate of fractal dimension D is composed of identical spherical monomers, each of radius a_0 and refractive index n_0 . The aggregate is immersed in a medium of refractive index $n_{\rm m}$ that fills the pores. Provided that both the monomers and the pores are substantially smaller than the wavelength of light, this composite structure may be modeled as a continuous medium whose refractive index, $n_{\rm p}$, is given by the Maxwell Garnett relation, $n_{\rm p}$ 0

$$L(n_{\rm p}) = \phi_{\rm p} L(n_{\rm 0}),\tag{3a}$$

where $\phi_{\rm p}$ is the volume fraction of monomers in the sphere and

$$L(n) = \frac{n^2 - n_{\rm m}^2}{n^2 + 2n_{\rm m}^2} \tag{3b}$$

is the Lorentz-Lorenz factor.

The number of monomers within radius r of a fractal aggregate's center is

$$N(r) = \left(\frac{r}{a_0}\right)^D,\tag{4}$$

and the associated volume fraction is

$$\phi(r) = \frac{a_0^3}{r^3} N(r) = \left(\frac{r}{a_0}\right)^{D-3}.$$
 (5)

For a particle of radius a_p , the overall volume fraction is

$$\phi_{\rm p} \equiv \phi(a_{\rm p}) = \left(\frac{a_{\rm p}}{a_0}\right)^{D-3}.\tag{6}$$

From this and the Maxwell Garnett relation, we obtain an expression for the cluster's effective refractive index,

$$n_{\rm p} = \sqrt{\frac{1 + 2L(n_0)\phi_{\rm p}}{1 - L(n_0)\phi_{\rm p}}}.$$
 (7)

This result also may be expressed as a scaling relationship between the radius of a fractal aggregate and its effective refractive index,

$$\ln L(n_{\rm p}) - \ln L(n_0) = (D-3) \ln \left(\frac{a_{\rm p}}{a_0}\right).$$
 (8)

In a population of aggregates grown under comparable conditions, eqn (8) can be used to estimate the population-averaged fractal dimension, *D*.

Eqn (7) treats a cluster as a homogeneous medium. In fact, the density of monomers decreases with scale, and therefore with radius within the cluster. As discussed in the Appendix, the associated radial gradient in the refractive index has little influence on practical measurements of clusters' effective characteristics. We, therefore, ignore the clusters' spatial inhomogeneity in the discussion that follows.

4 Experimental studies of model fractal aggregates

4.1 Fractal aggregates of polystyrene nanospheres

The data in Fig. 3 were obtained for 2727 colloidal fractal aggregates grown under conditions conducive to diffusion-limited cluster aggregation (DLCA).^{22–24} The primary particles are monodisperse

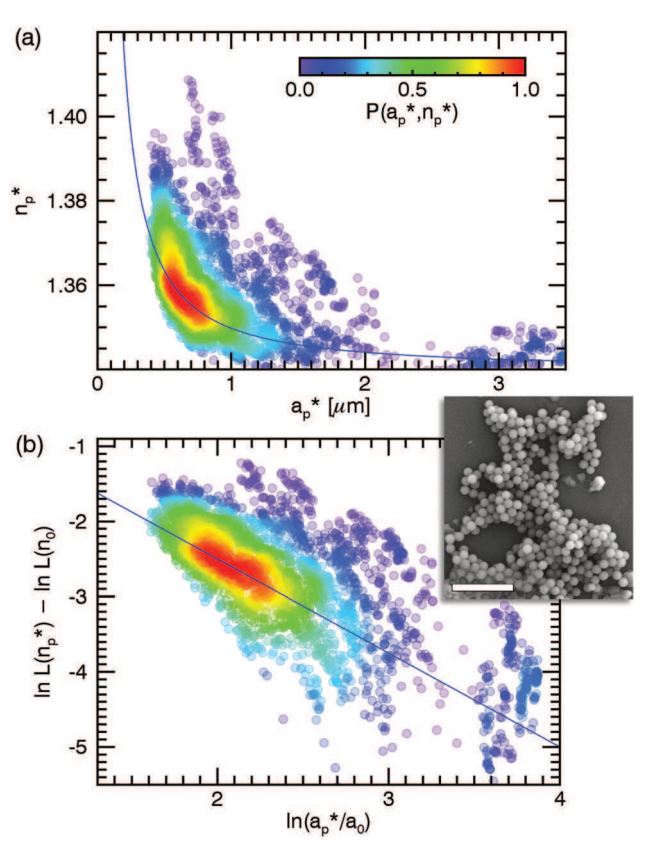


Fig. 3 Characterization data for a population of polystyrene fractal aggregates. (a) Scatter plot of the effective radius, $a_{\rm p}^*$, and refractive index, $n_{\rm p}^*$, of 2727 aggregates, including the example from Fig. 1(a). Each plot symbol reflects the properties of one aggregate, and is colored by the relative probability density of measurements, $P(a_{\rm p}^*, n_{\rm p}^*)$. The solid (blue) curve is the prediction of eqn (8) using the fractal dimension D=1.75 for diffusion-limited cluster aggregation, and no other adjustable parameters. (b) The same data replotted for comparison with the scaling prediction from eqn (8). According to the effective-sphere model, the rescaled data are expected to fall along the solid (blue) line. Inset: Scanning electron microscope image of a typical aggregate. Scale bar indicates 1 μ m.

Paper Soft Matter

polystyrene spheres with a mean radius of a_0 = 80 nm (Thermo Scientific, catalog number 5016A, 10% w/w).

Aggregation was initiated by dispersing these particles in 0.5 M NaCl solution at a concentration of 5×10^{-5} by weight. After one hour, the dispersion was diluted by a factor of 20 with deionized water to stop further aggregation. The resulting sample was then analyzed immediately, before the aggregates might have time to restructure. ^{24,25}

Each data point in Fig. 3(a) represents the characteristics of a single colloidal particle obtained from a trajectory such as the example in Fig. 2. The plot symbols' size is comparable to the numerical uncertainty in the fit parameters. Each point is colored according to the relative probability density, $P(a_p^*, n_p^*)$, of measurements according to the color bar inset into Fig. 3(a).

The effective sphere model works well for aggregates with radii smaller than 2 μ m. Despite their irregular shapes, these objects are small enough that their holograms display the radial symmetry typical of spheres. This can be seen in Fig. 3(b). The reduced χ^2 statistics for fits such as Fig. 3(c) typically fall within ten percent of unity, suggesting that the fit parameters reliably reflect the aggregates properties.

Larger aggregates are reliably detected and counted by the feature identification algorithm, ¹⁶ but are poorly characterized by the effective-sphere model. ⁸ Their holograms are more substantially asymmetric, and the reduced χ^2 statistic for these fits typically exceeds 10. It is not surprising, therefore, that the estimated characteristics for aggregates with $a_{\rm p}>2.5~\mu{\rm m}$ do not follow the trend expected for fractal aggregates, their refractive indexes falling below the scaling prediction.

The solid curve in Fig. 3(a) shows the prediction from eqn (8) for $n_{\rm p}(a_{\rm p})$, with no adjustable parameters. In addition to the monomers' radius, the effective-sphere model is parametrized by the monomers' refractive index and the clusters' fractal dimension. The former, $n_0 = 1.59 \pm 0.01$, was obtained from holographic characterization studies of emulsion-polymerized polystyrene spheres. The latter, $D = 1.75 \pm 0.03$, was obtained from independent light-scattering studies on aggregates grown under comparable conditions, and is consistent with expectations for DLCA.

Fig. 3(b) shows the same data replotted to emphasize the scaling prediction from eqn (8). Agreement with the effective sphere model is quite good for particles with apparent radii smaller than $a_{\rm p}^*=2~\mu{\rm m}$. Because fractals' pore size increases with scale, larger aggregates presumably do not satisfy the requirements of effective medium theory and so are not so well described by the effective-sphere model.

The scanning electron microscope image inset into Fig. 3(b) shows a typical vacuum-dried aggregate. This image resolves the individual spheres, whose arrangement is consistent with the irregular branched structure inferred from holographic characterization of similar samples. Although details of the structure undoubtedly were altered during drying, the presence of voids at multiple scales within the cluster is consistent with a fractal dimension smaller than 2.

The model's success for smaller clusters supports the contention that eqn (8) can be useful for measuring the

population-averaged fractal dimension of micrometer-scale fractal clusters. We next apply this approach to characterize aggregates of two model proteins whose cluster morphologies have been independently established. This application not only serves to verify the effective-sphere model for fractal clusters, but also illustrates the utility of Lorenz–Mie microscopy for measuring the size distribution and morphology of protein aggregates, a subject of considerable interest in biology³⁰ and of substantial practical importance in pharmaceutical manufacturing.³¹

4.2 Protein aggregates

Like the colloidal nanoparticles considered in the previous section, proteins in solution also have a tendency to aggregate. Some of the resulting macromolecular structures perform important biological functions. Others cause diseases. Protein aggregation is a principal failure mechanism for biopharmaceutical formulations not only because clustered proteins are less effective as therapeutic agents, but also because they can elicit dangerous immune responses. We previously have demonstrated that inline holographic video microscopy can detect protein aggregates in solution, and can distinguish them from such common contaminants as silicone oil droplets. Here, we apply the effective-sphere model to study the aggregates' morphology by estimating their fractal dimension.

4.2.1 Bovine insulin. The data in Fig. 4(a) were obtained for aggregates of bovine pancreas insulin ($M_{\rm w}$: 5733.49 Da, Sigma-Aldrich, CAS number: 11070-73-8) that were prepared according to previously published methods. ^{32,33} Insulin was dissolved at a concentration of 5 mg mL⁻¹ in 10 mM Tris buffer (Life Technologies, CAS number 77-86-1). The pH of the buffer was adjusted to 7.4 with 37% hydrochloric acid (Sigma Aldrich, CAS number: 7647-01-0). The solution then was centrifuged at 250 rpm for 1 h to induce aggregation, at which time the sample still appeared transparent to visual inspection.

Running 100 μ L of this sample through the holographic characterization instrument reveals a concentration of 3.9 \pm 0.1 \times 10⁷ aggregates per mL, including the examples whose properties are plotted in Fig. 4(a). Because the effective monomer radius is not known *a priori*, radii in Fig. 4 are scaled by an arbitrary factor, $a_0 = 1$ μ m. This choice does not affect the estimate for *D*.

The main distribution of single-particle characteristics follows the scaling prediction quite well, and has a slope consistent with a fractal dimension of D = 1.5. This is denoted in Fig. 4(a) by a solid (red) line superimposed on the data.

Dashed lines in this plot show equivalent results for fractal dimensions D=1.4 and D=1.6. The proposal that bovine insulin forms branched fractal aggregates is consistent with independent measurements of such aggregates' morphology using atomic-force microscopy.³⁴

In addition to the main distribution of points, Fig. 4(a) features an outlying cluster of large-size aggregates comparable to those in Fig. 3. It also includes a cluster of small particles with low refractive indexes. These latter features appear to correspond to globular aggregates that are distinct from the fractal clusters of interest here.

Soft Matter Paper

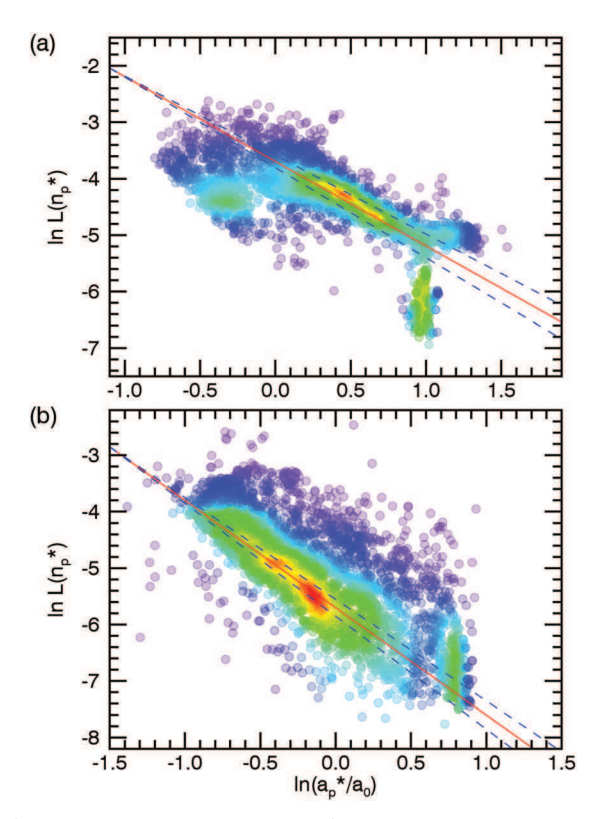


Fig. 4 Lorenz–Mie characterization of protein aggregates, plotted to emphasize the scaling prediction of eqn (8). Radii are measured relative to the arbitrary scale, $a_0 = 1 \, \mu \text{m}$. Each point represents the properties of a single colloidal particle and is colored according to the local density of measurements. Superimposed (red) lines corresponds to the best-fit fractal dimension for each sample, with dashed lines indicating a range of ± 0.1 . (a) Bovine pancreas insulin. The data are consistent with $D = 1.5 \pm 0.1$. (b) Bovine serum albumin. The distribution is consistent with $D = 1.1 \pm 0.1$.

4.2.2 Bovine serum albumin. Solutions of bovine serum albumin (BSA) ($M_{\rm w}$: 66 500 Da, Sigma Aldrich, CAS number: 9048-46-8) were aggregated by complexation with poly(allylamine hydrochloride) (PAH) ($M_{\rm w}$: 17 500 g mol $^{-1}$, CAS number: 71550-12-4, average degree of polymerization: 1207). ^{35,36} BSA and PAH were dissolved in 10 mM Tris–HCl buffer (pH 7.4) (Life Technologies, CAS number: 77-86-1) to achieve concentrations of 1.22 mg mL $^{-1}$ and 0.03 mg mL $^{-1}$, respectively. The reagents were mixed by vortexing to ensure dissolution, and aggregates formed after the sample was allowed to equilibrate for one hour.

Holographic characterization data for a sample of BSA–PAH complexes, shown in Fig. 4(b), reveal $9.8\pm0.5\times10^6$ aggregates per mL in the range of radii running from 300 nm to $2.5~\mu m$, and a peak radius of $0.5~\mu m$. Although our implementation of holographic characterization is capable of detecting aggregates with radii up to $10~\mu m$, no aggregates were observed with radii exceeding $2.5~\mu m$. The results for BSA aggregates with radii smaller than $2~\mu m$ agree well with the scaling prediction from eqn (8), this time with an apparent fractal dimension of D=1.1, as indicated by the solid (red) line superimposed on the data in Fig. 4(b). The nearly linear structure suggested by this low fractal dimension is consistent with atomic force microscopy images of BSA aggregates. 37

5 Conclusions

The experimental results presented in Section 4 demonstrate that Lorenz–Mie microscopy can provide useful insights into the properties of micrometer-scale fractal aggregates. Holograms of micrometer-scale colloidal fractal aggregates can be interpreted with the effective-sphere model presented in Section 3 to estimate an aggregate's size and effective refractive index. These particle-resolved data, in turn, can be pooled to estimate the population-averaged fractal dimension. The effective-sphere model therefore extends the particle-characterization capabilities of Lorenz–Mie microscopy to irregularly branched objects.

The success of the effective-sphere model in characterizing ramified protein aggregates lends additional support to the earlier proposal⁸ that Lorenz–Mie characterization meaningfully assesses such aggregates' sizes. It therefore establishes Lorenz–Mie microscopy as a method for sizing protein aggregates, characterizing their morphology, and differentiating them from other types of colloidal particles.

This work also provides a baseline against which more detailed approaches to holographic characterization of fractal structures may be compared. Future extensions based on machine-learning techniques³ or direct modeling of the spatial distribution of dielectric material⁴ thus can be tested directly using the methods described here.

Appendix: Effective-sphere model for gradient-index spheres

The effective-sphere model treats an aggregate as if the monomers were distributed uniformly within it. In fact, the marginal volume fraction decreases with distance r from the center of the aggregate as

$$\phi_{s}(r) = \frac{\frac{4}{3}\pi a_0^3}{4\pi r^2} \frac{dN}{dr} = \frac{D}{3} \left(\frac{r}{a_0}\right)^{D-3}.$$
 (9)

This corresponds to a radial variation of the effective refractive index described by

$$n(r) = n_{\rm m} \sqrt{\frac{1 + 2L(n_0)\phi_{\rm s}(r)}{1 - L(n_0)\phi_{\rm s}(r)}}.$$
 (10)

Unless the entire aggregate is smaller than the wavelength of light, this radial structure might be expected to influence results obtained by applying effective medium theory to holograms of fractal aggregates.

To assess this influence, we use the effective-sphere model to analyze synthetic holograms of gradient-index particles with refractive-index profiles described by eqn (10). These holograms are computed by replacing $\mathbf{f}_{\rm s}(k\mathbf{r}|a_{\rm p},n_{\rm p})$ in eqn (2) with the corresponding generalized Lorenz–Mie result for a stratified sphere^{38–40} whose layers have refractive indexes given by eqn (10). The number of layers is chosen to converge the computed intensities to within 1% at each pixel. This typically occurs with layer thicknesses comparable to $\pi/(5k)$. A similar

Paper Soft Matter

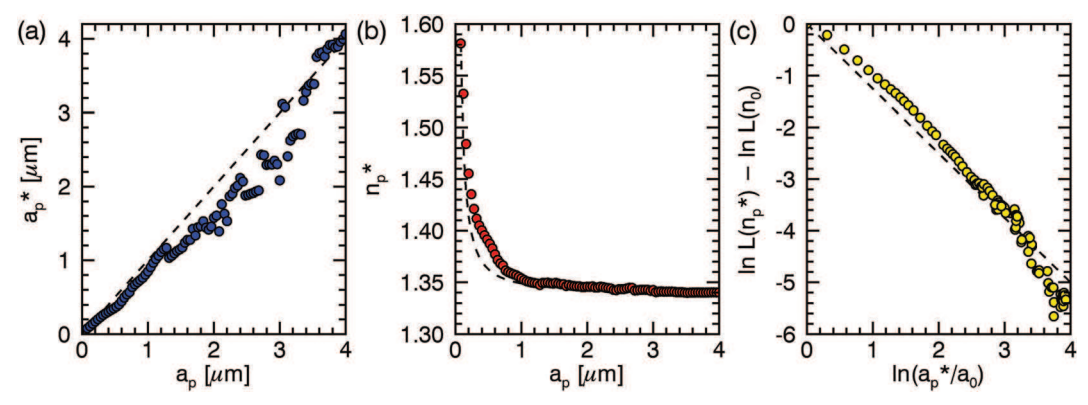


Fig. 5 Performance of the effective-sphere model for gradient-index spheres. (a) Effective radius, a_p *, as a function of the stratified sphere's outer radius, a_p . The dashed diagonal line indicates ideal agreement. (b) Effective refractive index, n_p *, as a function of sphere radius. The dashed curve indicates the sphere-averaged refractive index, n_p . (c) Scaling plot of the data, plotted according to eqn (8). The dashed diagonal line is obtained for the true values of radius and refractive index.

approach has proved successful for Luneburg spheres and other particles with continuous radial refractive index profiles. ⁴¹ The hologram is then fit to the Lorenz–Mie model from eqn (2) for the effective sphere's radius, a_p^* , and refractive index, n_p^* . These parameters then can be compared with the true radius of the stratified sphere, a_p , and the sphere-averaged refractive index, n_p , obtained from eqn (8).

Fig. 5 shows the performance of the effective-sphere model for particles with D=1.75, $a_0=80$ nm and $n_0=1.585$ in a medium with $n_{\rm m}=1.340$. These parameters are chosen to model fractal polystyrene aggregates dispersed in water. ^{23,24,28} The effective sphere's radius, Fig. 5(a), and refractive index, Fig. 5(b), both track the true values, albeit with systematic offsets. They quite closely satisfy the anticipated scaling form predicted by eqn (8) with a slope consistent with the input fractal dimension, as can be seen in Fig. 5(c).

Comparable results are obtained with different values of the fractal dimension. The gradient-index structure of fractal aggregates therefore does not substantially diminish the ability of the effective-sphere model to estimate such particles' fractal dimension. Although the gradient-index model does not address the influence of real aggregates' branched structure, it lends additional confidence to the proposal that Lorenz–Mie characterization usefully assesses the properties of such objects.

Acknowledgements

This work was funded primarily by the National Institutes of Health under Grant Number 1R43TR001590. Additional support was provided by the MRSEC program of the National Science Foundation under Award Number DMR-1420073. The holographic characterization instrument used for this study was constructed with support of the MRI program of the NSF under Award Number DMR-0922680. The scanning electron microscope was purchased with financial support from the MRI program of the NSF under Award DMR-0923251. We are grateful to Prof. Andrew Hollingsworth for assistance with the SEM.

References

- 1 S.-H. Lee, Y. Roichman, G.-R. Yi, S.-H. Kim, S.-M. Yang, A. van Blaaderen, P. van Oostrum and D. G. Grier, *Opt. Express*, 2007, **15**, 18275–18282.
- 2 B. J. Krishnatreya, A. Colen-Landy, P. Hasebe, B. A. Bell, J. R. Jones, A. Sunda-Meya and D. G. Grier, *Am. J. Phys.*, 2014, 82, 23–31.
- 3 A. Yevick, M. Hannel and D. G. Grier, Opt. Express, 2014, 22, 26884–26890.
- 4 J. Fung, R. W. Perry, T. G. Dimiduk and V. N. Manoharan, J. Quant. Spectrosc. Radiat. Transfer, 2012, 113, 2482–2489.
- 5 F. C. Cheong, K. Xiao, D. J. Pine and D. G. Grier, *Soft Matter*, 2011, 7, 6816–6819.
- 6 C. Wang, H. W. Moyses and D. G. Grier, *Appl. Phys. Lett.*, 2015, **107**, 051903.
- 7 M. Hannel, C. Middleton and D. G. Grier, *Appl. Phys. Lett.*, 2015, **107**, 141905.
- C. Wang, X. Zhong, D. B. Ruffner, A. Stutt, L. A. Philips,
 M. D. Ward and D. G. Grier, *J. Pharm. Sci.*, 2016, 105, 1074–1085.
- 9 W. Wang, Int. J. Pharmacol., 2005, 289, 1-30.
- 10 J. Panchal, J. Kotarek, E. Marszal and E. M. Topp, *AAPS J.*, 2014, **16**, 440–451.
- 11 G. B. Basim and B. M. Moudgil, *J. Colloid Interface Sci.*, 2002, **256**, 137–142.
- 12 J. Sheng, E. Malkiel and J. Katz, *Appl. Opt.*, 2006, **45**, 3893–3901.
- 13 S.-H. Lee and D. G. Grier, Opt. Express, 2007, 15, 1505-1512.
- 14 C. F. Bohren and D. R. Huffman, *Absorption and Scattering of Light by Small Particles*, Wiley Interscience, New York, 1983.
- 15 M. I. Mishchenko, L. D. Travis and A. A. Lacis, *Scattering, Absorption and Emission of Light by Small Particles*, Cambridge University Press, Cambridge, 2001.
- 16 B. J. Krishnatreya and D. G. Grier, *Opt. Express*, 2014, 22, 12773–12778.
- 17 F. C. Cheong, B. Sun, R. Dreyfus, J. Amato-Grill, K. Xiao, L. Dixon and D. G. Grier, *Opt. Express*, 2009, 17, 13071–13079.

Soft Matter Paper

- 18 L. Dixon, F. C. Cheong and D. G. Grier, *Opt. Express*, 2011, **19**, 4393–4398.
- 19 J. C. Crocker and D. G. Grier, J. Colloid Interface Sci., 1996, 179, 298–310.
- 20 D. E. Aspnes, Am. J. Phys., 1982, 50, 704-709.
- 21 T. C. Choy, Effective Medium Theory: Principles and Applications, Oxford University Press, New York, 1999.
- 22 P. Meakin, Adv. Colloid Interface Sci., 1988, 28, 249-331.
- 23 D. Majolino, F. Mallamace, P. Migliardo, N. Micali and C. Vasi, Phys. Rev. A: At., Mol., Opt. Phys., 1989, 40, 4665–4674.
- 24 Z. Zhou and B. Chu, *Physica A*, 1991, 177, 93–100.
- 25 C. Aubert and D. S. Cannell, *Phys. Rev. Lett.*, 1986, **56**, 738–741.
- 26 K. Xiao and D. G. Grier, Phys. Rev. E: Stat., Nonlinear, Soft Matter Phys., 2010, 82, 051407.
- 27 C. M. Sorensen, Aerosol Sci. Technol., 2001, 35, 648-687.
- 28 H. Wu, M. Lattuada and M. Morbidelli, *Adv. Colloid Interface Sci.*, 2013, **195-196**, 41–49.
- 29 D. A. Weitz, J. S. Huang, M. Y. Lin and J. Sung, *Phys. Rev. Lett.*, 1985, 54, 1416–1419.
- 30 A. M. Morris, M. A. Watzky and R. G. Finke, *Biochim. Biophys. Acta*, 2009, **1794**, 375–397.

- 31 W. Wang, Int. J. Pharm., 1999, 185, 129-188.
- 32 V. Sluzky, J. A. Tamada, A. M. Klibanov and R. Langer, *Proc. Natl. Acad. Sci. U. S. A.*, 1991, **88**, 9377–9381.
- 33 H. R. Costantino, R. Langer and A. M. Klibanov, *Pharm. Res.*, 1994, **11**, 21–29.
- 34 K. Siposova, M. Kubovcikova, Z. Bednarikova, M. Koneracka, V. Savisova, A. Antosova, P. Kopcansky, Z. Daxnerova and Z. Gazova, J. Nanotechnol., 2012, 23, 055101.
- 35 V. Ball, M. Winterhalter, P. Schwinte, P. Lavalle, J.-C. Voegel and P. Schaaf, *J. Phys. Chem. B*, 2002, **106**, 2357–2364.
- 36 T. Hagiwara, H. Kumagai and K. Nakamura, *Biosci., Biotechnol., Biochem.*, 1996, **60**, 1757–1763.
- 37 M. Omichi, A. Asano, S. Tsukuda, K. Takano, M. Sugimoto, A. Saeki, D. Sakamaki, A. Onoda, T. Hayashi and S. Seki, *Nat. Commun.*, 2014, 5, 3717.
- 38 W. Yang, Appl. Opt., 2003, 42, 1710-1720.
- 39 O. Pena and U. Pal, Comput. Phys. Commun., 2009, 180, 2348-2354.
- 40 G. Gouesbet and G. Gréhan, *Generalized Lorenz-Mie Theories*, Springer-Verlag, Berlin, 2011.
- 41 M. Selmke, *J. Quant. Spectrosc. Radiat. Transfer*, 2015, **162**, 175–183.